



# Influence of Radiation and Convection on 3D-Casson Hybrid Nanofluid Flow in the Presence of Suction Over a Rotary Sheet

Alfunsa Prathiba\*<sup>1</sup>  and A. V. Lakshmi<sup>2</sup> 

<sup>1</sup> Department of Humanities and Sciences, CVR College of Engineering, Mangalpally, Telangana, India

<sup>2</sup> Department of Mathematics, Osmania University, Hyderabad, India

\*Corresponding author: [alphonsaperli@gmail.com](mailto:alphonsaperli@gmail.com)

Received: April 7, 2022

Accepted: August 6, 2022

**Abstract.** The current research looks at how the radiation affects the convective hybrid Casson 3D flow in the presence of suction. The fluid analysed was a hybrid nanofluid made up of Alumina ( $\text{Al}_2\text{O}_3$ ) and Copper (Cu) nanoparticles diffused in base fluid (Water). After simplification, the flow control equations were programmed and solved employing the MATLAB software and the `bvp4c` code. Figures depict the study's most important findings, such as the impact of several physical elements such as convection, radiation, and suction on the velocity profile, mass transfer, temperature field, friction factor, and heat transfer coefficient. According to the key findings, the Casson Hybrid nanofluid has a better property than normal fluids. It can also be deduced that as the scale of the radiation constraint strengthens, the temperature field improves. Tables were used to validate our findings with cited papers.

**Keywords.** Richardson number, Radiation, Suction, Hybrid Casson fluid, Rotating sheet, Heat source

**Mathematics Subject Classification (2020).** 76A05, 76A10, 76Dxx, 76R10, 76R50, 76Uxx

Copyright © 2022 Alfunsa Prathiba and A. V. Lakshmi. This is an open access article distributed under the Creative Commons Attribution License, which permits unrestricted use, distribution, and reproduction in any medium, provided the original work is properly cited.

## 1. Introduction

In a general sense, “non-Newtonian modeling” has a non-linear correlation between the rate of strain and stress. Non-Newtonian fluids’ mechanical properties, such as shear thickness or thinness, normal stress variation, and visco-elastic reactivity, may not be adequately represented

by traditional theories, necessitating a new and effective estimate. To explain the movement and heat transmission mechanisms, various constitutive non-Newtonian models have been anticipated. One of them is the Casson model, which has sparked a lot of curiosity. Despite its difficulties, engineers and applied mathematicians are interested in the NNF mechanism for flow and heat transfer properties. Biotechnology, metallurgy, medicine development, and chemical engineering, among other industries, rely on these fluids [26]. Casson fluid is a Newtonian fluid with variable viscosity [42] that has specific characteristics and has subsequently become rather famous. Casson [6] developed the Casson fluid model in 1959 to estimate the flow performance of “pigment-oil suspensions”. So, for flow, the Casson fluid’s magnetic shear stress must be greater than the yield shear stress, or the fluid will act like an inflexible body. This type of fluid is classified as purely viscous and has a high viscosity. The Casson model relies on a structure model of two-phase suspensions’ interacting behaviour of solid and liquid phases. Jelly, sauce, tomato, honey, soup are few examples of Casson fluid. The presence of fibrinogen, protein, and globulin in aqueous base plasma and human red blood cells, human blood can also be treated as Casson fluid. The Casson fluid solutions are obtained in most of the research using either an approximation method or a numerical scheme. Khan *et al.* [23] explored the computer-generated examination of “Casson fluid through homogeneous and heterogeneous processes”. Sohail *et al.* [49] implemented the OHAM method to investigate the “entropy generation in electrically conducted Casson fluid in thermal conductivity across a bi-directional elongating sheet”. The effects of radiation on a Casson fluid moving across an exponentially extending plane was conducted by Seini *et al.* [45]. Numerous investigations on the momentum, “heat, and mass transfer” of Casson fluids under diverse conditions have been conducted by a variety of investigators using numerical or analytical techniques, as evidenced by the references [7, 8, 18, 25, 30, 31, 35, 41].

Advanced liquids like “Nano fluorescence” have replaced traditional heat transfer fluids because they increase a fluid’s heat transmission and flow characteristics [19]. Nanoparticles in the heat exchanger reduce the heat exchanger’s volume and bulk while lowering the water flow. Many researchers looked at the use of nanofluid in heat exchangers. It has resulted in a significant boost in performance. In the inception, nanoparticles were utilised by Hayat *et al.* [16] to improve the heat capacity and temperature distribution of fluids.

On the other hand, recent technological improvements have necessitated an innovative revolution in heat transport. In recent years, nanofluid research has exploded, with results revealing that the fluids containing the nanoparticles are excellent heat transferring fluids. These fluids have research and industrial applications. The thermal and mechanical properties are influenced by the carrier fluid composition, nanomaterial dissemination, particle type, size, and manufacturing procedures. During persistent particle volume concentration and flow emissions, the heat transport improvement is based on the thermal characteristics of the nanoparticles [43]. Creating hybrid nanoparticles can change the thermal conductivity of nanoparticles or make them better at it. It’s possible to make “hybrid nanofluids (HNF)” by

putting together a lot of different metal nanoparticles with the base fluid [26]. These HNF flows are a novel type of nanofluid that could be employed in microfluidics, manufacturing, logistics, health services, marine architecture, and acoustics, among other applications. When nano-sized nanoparticles are disseminated correctly, hybrid nanoparticles have a very high effective heat conductivity, which is a big benefit. Nanofluid flow is superior to conventional fluid flow because it can transport a large amount of heat. As a result, HNF is being utilised more frequently to increase heat conductivity [16]. As a result of this breakthrough, researchers began to report various issues related to HNF shortly after they were introduced.

Darcy's model was used for the numerical analysis of water-based hybrid nanofluids by Gireesha *et al.* [12]. According to this study, fins with identified convective coefficients at the tip transmit heat more quickly than those with insulated tips. RKF-45 was used by Sarwe *et al.* [44] to examine the "effect of magnetic and Arrhenius activation energy on the flow of Casson hybrid nanofluid over a vertically moving plate". Devi and Devi [9] investigated 3D HNF (Cu-Al<sub>2</sub>O<sub>3</sub>/water) flows by implementing the numerical simulations over the "Lorentz force tensile sheets under Newtonian heating". Sundar *et al.* [51] show that HNF is more efficient heat carrying fluids than single nanoparticle traditional fluids. Jamshed *et al.* [20], and Ellahi [10] offered a complete and extensive examination of deterministic and HNF with NNF heat transmission and entropy development investigations. Further, sources of HNF in the focus of MHD can also be uncovered in the existing works [13, 34, 48, 50, 53].

Engineers and physicists were encouraged to investigate the flow across a rotating frame by its practical and theoretical applications. The flow of mantle near the crust and the flow of geological formations exposed owing to the earth's rotation sparked the interest in rotatory flows. Centrifugal filters, rotating machinery, and food processing all use these streams. Wang [54] presented an innovative study of 3D rotary viscous flow. His problem was governed by a gravitational parameter representing the rotational speed/ extension ratio. He implemented the usual perturbation method to generate the series solution. Later many researchers have extended this study under different boundary conditions and over various fields [1–3, 22, 24, 36, 39, 40, 46, 52]. Heat transport improvement with "Ag-Cu O/water HNF" was performed by Hayat and Nadeem [15]. Their study concluded that the radiation, heat source, and chemical effect, the heat transport rate of HNF is greater than that of plain nanofluid. Shoaib *et al.* [47] have studied the trend of heat and mass transmission in the 3D flow of HNF over a rotational disk under the influence of radiation and noticed that heat transfer rate was related to the "Brinkman number".

Technical applications such as microfibre coating, projectile motion, and rotary machinery design for re-entry rockets rely on heat transfer and flow on rotating devices of rotation in a forced flow. There has been no numerical analysis of the thermophysical parameters for an "elongating sheet with convection, radiation, heat generation, and suction effects" of a 3D rotating Casson HNF. Consequently, the current work is devoted to examining these consequences. Similarity transformations are used to simplify the phase flow HNF model's

governing PDEs. The reduced equations are then numerically evaluated using MATLAB's finite difference scheme, which executes the 3-stage Lobatto IIIA formula [28]. Finally, we present our numerical results in figures and tables.

## 2. Mathematical Formulation

Consider a 3D spinning and incompressible Casson HNF across a stretched sheet influenced by convection, radiation, and suction. The stretching sheet is supposed to stretch linearly along the  $x$ -axis at a velocity  $U = ax$ , and  $a$  is a constant and the considered fluid is positioned on the  $z$ -axis. The velocity components in the  $(x, y, z)$  directions are assumed to be  $(u, v, w)$ . The fluid and sheet rotate at a uniform angular velocity  $\Omega$  around the  $z$ -axis, as shown in Figure 1. The surface and ambient temperatures are denoted by  $T_w$  and  $T_\infty$ , respectively, whereas the species concentrations at the wall and infinity are denoted by  $C_w$  and  $C_\infty$ , individually.

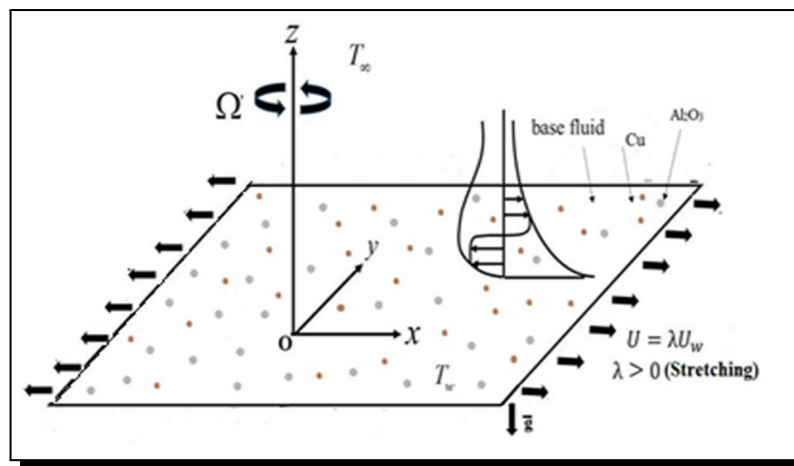


Figure 1. Physical outline of the flow

The necessary “rheological equations of Cauchy stress tensors for anisotropic and incompressible fluid flow of a Casson” form could be stated as follows [4],

$$\tau_{ij} = \begin{cases} 2 \left( \mu_B + \frac{p_y}{\sqrt{2\pi}} \right) e_{ij}, & \pi > \pi_c, \\ 2 \left( \mu_B + \frac{p_y}{\sqrt{2\pi_c}} \right) e_{ij}, & \pi < \pi_c, \end{cases} \quad (2.1)$$

where  $\tau_{ij}$  is the *Cauchy stress tensor*,  $\pi = (e_{ij})^2$  is the deformation rate components product with itself,  $e_{ij}$  is the  $(i, j)$ th contort rate component,  $\pi_c$  is the critical value,  $\mu_B$  is the “plastic dynamic viscosity” [21], and  $p_y$  is the fluid yield stress [5]. In the present problem, the stress component is considered as,

$$\tau_{xz} = \mu_B \left( 1 + \frac{1}{\beta} \right) \left( \frac{\partial w}{\partial x} + \frac{\partial u}{\partial z} \right) \quad \text{and} \quad \frac{\partial w}{\partial x} = 0, \quad \text{where } \beta = \mu_B \frac{\sqrt{2\pi_c}}{p_y}.$$

$\beta$  is Casson fluid parameter.

In a rotating frame, the boundary layer equations governing equations (making use of Rosseland approximations for non-linear thermal radiation) are given by [4, 26, 29, 44].

The conservation of mass,

$$\frac{\partial u}{\partial x} + \frac{\partial v}{\partial y} + \frac{\partial w}{\partial z} = 0. \tag{2.2}$$

The momentum equation,

$$u \frac{\partial u}{\partial x} + v \frac{\partial u}{\partial y} + w \frac{\partial u}{\partial z} = \left(1 + \frac{1}{\beta}\right) \frac{\mu_{hnf}}{\mu_{nf}} \frac{\partial^2 u}{\partial z^2} + 2\Omega v + g\beta_{hnf}(T - T_\infty), \tag{2.3}$$

$$u \frac{\partial v}{\partial x} + v \frac{\partial v}{\partial y} + w \frac{\partial v}{\partial z} = \left(1 + \frac{1}{\beta}\right) \frac{\mu_{hnf}}{\mu_{nf}} \frac{\partial^2 v}{\partial z^2} - 2\Omega u. \tag{2.4}$$

The energy equation,

$$u \frac{\partial T}{\partial x} + v \frac{\partial T}{\partial y} + w \frac{\partial T}{\partial z} = k_{hnf} \frac{\partial^2 T}{\partial z^2} + \frac{16\sigma_0 T_\infty^3}{3k^*(\rho C_p)_{hnf}} \frac{\partial^2 T}{\partial z^2} + \frac{Q_0(T - T_\infty)}{(\rho C_p)_{hnf}}. \tag{2.5}$$

The concentration equation,

$$u \frac{\partial C}{\partial x} + v \frac{\partial C}{\partial y} + w \frac{\partial C}{\partial z} = D_{hnf} \frac{\partial^2 C}{\partial z^2}. \tag{2.6}$$

The supposed initial and boundary conditions of the flow concerned are,

$$\left. \begin{aligned} u = U_w \lambda = \alpha x \lambda, \quad v = 0, \quad w = w_w, \\ T = T_w, \quad C = C_w \quad \text{at } z = 0 \\ u \rightarrow 0, \quad v \rightarrow 0, \quad w \rightarrow 0, \quad T \rightarrow T_\infty, \\ C \rightarrow C_\infty \quad \text{as } z \rightarrow \infty \end{aligned} \right\} \tag{2.7}$$

Here, “ $\lambda$  is the stretching and shrinking parameter taking a constant value such that  $\lambda > 0$  for the stretching;  $\lambda < 0$  for the shrinking; and  $\lambda = 0$  for the static sheet” [3].

### 3. Method of Solution

The transformations of similarity that meet the equation of continuity (2.2) and to convert the PDEs’ (2.3)-(2.6) to ODE can be identified as [3],

$$\left. \begin{aligned} u = \alpha x F'(\eta), \quad v = \alpha x G(\eta), \quad w = -\sqrt{a \vartheta_f} F(\eta), \\ \Theta(\eta) = \frac{T - T_\infty}{T_w - T_\infty}, \quad \Phi(\eta) = \frac{C - C_\infty}{C_w - C_\infty}, \quad \eta = z \sqrt{\frac{a}{\vartheta_f}} \end{aligned} \right\} \tag{3.1}$$

such that  $w_w = -\sqrt{a \vartheta_f} S$  and the prime in the above equations indicates the derivative relating to  $\eta$  and  $S$  is the “mass flux parameter” in which  $S < 0$  indicates injection and  $S > 0$  corresponds to suction.

Applying the transformations in equation (3.1) to equations (2.3)-(2.6), we obtain the transformed equations as,

$$\left(1 + \frac{1}{\beta}\right) \frac{\mu_{hnf}}{\rho_{hnf}} \frac{\rho_f}{\mu_f} F'''' + \frac{(\rho\beta)_{hnf}}{\rho_{hnf} \beta_f} R_i \Theta + F'' F + 2\omega G - (F')^2 = 0, \tag{3.2}$$

$$\left(1 + \frac{1}{\beta}\right) \frac{\mu_{hnf}}{\rho_{hnf}} \frac{\rho_f}{\mu_f} G'' - F' G + F G' - 2\omega F = 0, \tag{3.3}$$

$$\frac{(\rho C_p)_f}{(\rho C_p)_{hnf}} \left\{ \frac{1}{Pr} \left[ \frac{k_{hnf}}{k_f} + \frac{4}{3} R_d \right] \Theta'' + \delta \Theta \right\} + F \Theta' = 0, \tag{3.4}$$

$$\Phi'' + \frac{D_f}{D_{hnf}} Sc F \Phi' = 0, \tag{3.5}$$

subject to the modified boundary condition,

$$\left. \begin{aligned} F'(\eta) = \lambda, G(\eta) = 0, F(\eta) = S, \Theta(\eta) = 1, \Phi(\eta) = 1 \text{ at } \eta = 0 \\ F'(\eta) \rightarrow 0, G(\eta) \rightarrow 0, \Theta(\eta) \rightarrow 0, \Phi(\eta) \rightarrow 0 \text{ as } \eta \rightarrow \infty \end{aligned} \right\} \tag{3.6}$$

The factors such as the rotation parameter ( $\omega$ ), the heat source/sink parameter ( $\delta$ ), Richardson number ( $Ri$ ), Prandtl number ( $P_r$ ), Schmidt parameter ( $Sc$ ) in the above equations can be presented as

$$Ri = \frac{Gr}{Re^2} = \frac{\beta_f g(T - T_\infty)x^3}{\vartheta_f^2 Re^2}, \omega = \frac{\Omega}{\alpha}, P_r = \frac{\nu_f}{\alpha_f}, Sc = \frac{\nu_f}{D_f}, \delta = \frac{Q_o}{\alpha_f(\rho C_p)_f}$$

when it comes to applications, it's important to know the x- and y-axis drag coefficients, the local "Nusselt number", and the "local Sherwood number", all of which are defined as

$$\begin{aligned} Re_x^{1/2} C_{fx} &= \frac{\mu_{hnf}}{\mu_{nf}} \left(1 + \frac{1}{\beta}\right) F''(0), \\ Re_x^{1/2} C_{fy} &= \frac{\mu_{hnf}}{\mu_{nf}} \left(1 + \frac{1}{\beta}\right) G'(0), \\ Re_x^{-1/2} Nu_x &= - \left[ \frac{k_{hnf}}{k_f} + \frac{4}{3} R_d \right] \Theta'(0), \\ Re_x^{-1/2} Sh_x &= - \frac{k_{hnf}}{k_{nf}} \Phi'(0) \end{aligned}$$

The subscripts  $f$ ,  $nf$  and  $hnf$  denote attributes of the base fluid, nanofluid, and HNF, respectively. Table 1 lists the thermophysical parameters of HNF, and the "hybrid theory and phenomenon commandment" recognises the efficient properties of HNF. The most important HNF experimental relationships are listed below.

**Table 1.** The thermophysical properties of water and the nanoparticles [33, 53]

| Properties  | Base fluid              | Nanoparticles                  |                         |
|---|-------------------------|--------------------------------|-------------------------|
|   | Water                   | Al <sub>2</sub> O <sub>3</sub> | Cu                      |
| Thermal conductivity ( $k$ )<br>(Wm <sup>-1</sup> K <sup>-1</sup> ) | 0.613                   | 40                             | 400                     |
| Density ( $\rho$ )<br>(Kgm <sup>-3</sup> )                          | 997.1                   | 3970                           | 8933                    |
| Specific heat ( $C_p$ ) (Jkg <sup>-1</sup> K <sup>-1</sup> )        | 4179                    | 765                            | 385                     |
| $\beta$ (1/K)   | 36.2 × 10 <sup>-5</sup> | 0.85 × 10 <sup>-5</sup>        | 1.67 × 10 <sup>-5</sup> |

The "Hamilton-Crosser model" [17], [37] (H.C) thermal conductivity model was employed to obtain the  $k_{hnf}$  and  $k_f$  relationships. The specific heats of Cu particles, Al<sub>2</sub>O<sub>3</sub> particles, base fluid, and hybrid liquid are provided in the thermophysical mathematical relations of the hybrid nanofluid  $(C_p)_{s1}$ ,  $(C_p)_{s2}$   $(C_p)_f$ ,  $(C_p)_{hnf}$ , respectively. The  $s_1$  denotes Al<sub>2</sub>O<sub>3</sub> properties,

while  $s_2$  denotes Cu properties. The HNF is made up of Alumina ( $Al_2O_3$ ) and Copper(Cu) nanoparticles dispersed in water ( $H_2O$ ). The nanoparticles' geometric size is spherical ( $m = 3$ ).  $\phi_1$  and  $\phi_2$  correspond to the nanoparticle volume share of Alumina ( $Al_2O_3$ ) and Copper(Cu), respectively, while  $\phi_{hnf}$  represents the mixed nanoparticle concentration. Throughout the study, the nanoparticle volume fraction of Alumina is kept constant at  $\phi_1 = 0.1$ .

The expressions for the main relationships such as thermal conductivity, “specific heat capacities at constant pressure”, density, and the “thermal expansion coefficient” are [11, 14],

$$\frac{\mu_{hnf}}{\mu_f} = \frac{1}{[(1 - \phi_1)(1 - \phi_2)]^{2.5}},$$

$$\frac{\rho_{hnf}}{\rho_f} = \left[ \left( \frac{\rho_{s1}}{\rho_f} \right) \phi_1 + (1 - \phi_1) \right] (1 - \phi_2) + \phi_2 \frac{\rho_{s2}}{\rho_{s1}},$$

$$[\rho C_p]_{hnf} = [\rho C_p]_f \left[ \left( \frac{(\rho C_p)_{s1}}{(C_p \rho)_f} \right) \phi_1 + (1 - \phi_1)(1 - \phi_2) + \phi_2 (\rho C_p)_{s2} \right],$$

$$\frac{k_{hnf}}{k_{bf}} = \frac{k_{bf}(m - 1) - (k_{bf} - k_{s2})(m - 1)\phi_2 + k_{s2}}{(k_{bf} - k_{s2})\phi_2 + k_{s2} + k_{bf}(m - 1)}$$

and

$$\frac{k_{bf}}{k_f} = \frac{k_{s1} + k_f(m - 1) - (k_f - k_{s1})(m - 1)\phi_1}{(k_f - k_{s1})\phi_2 + k_{s1} + k_f(m - 1)},$$

$$\left[ \left( \frac{\rho_{s1}\beta_{s1}}{\rho_f\beta_f} \right) \phi_1 + (1 - \phi_1) \right] (1 - \phi_2) + \phi_2 \frac{\rho_{s2}\beta_{s2}}{\rho_f\beta_f} = \frac{[\beta]_{hnf}}{[\beta]_f}.$$

### 4. Numerical Solution

The system of dimensionless equations from (3.2) to (3.5) is very sensitive to boundary conditions in math. These equations are so complicated that it's hard to solve them analytically. As a result, the BVP4C method from MATLAB is one of the ways to solve these kinds of problems. The MATLAB BVP algorithm bvp4c is used to get the numerical solutions. It is “a finite difference code that implements the three-stage Lobatto IIIA formula”.

First, the equations (3.2) to (3.5) are changed into a set of “coupled first-order equations”. As

$$f = [F \ F' \ F'' \ G \ G' \ \Theta \ \Theta' \ \Phi \ \Phi']^T$$

$$= \begin{bmatrix} f(1) \\ f(2) \\ f(3) \\ f(4) \\ f(5) \\ f(6) \\ f(7) \\ f(8) \\ f(9) \end{bmatrix}.$$

Therefore, the equations (3.2)-(3.5) can be expressed in linear form as

$$f'(3) = \frac{-A_1 A_2 [A_3 Ri f(6) + f(1)f(3) + 2\omega f(4) - f(2) * f(2)]}{\left(1 + \frac{1}{\beta}\right)},$$

$$f'(5) = \frac{-A_1 A_2 [f(2)f(4) + 2\omega f(2) - f(1)f(5)]}{\left(1 + \frac{1}{\beta}\right)},$$

$$f'(7) = \frac{-Pr(B_1 f(1)f(7) + \delta f(6))}{B_2 + \frac{4Rd}{3}},$$

$$f'(9) = -Sc B_3 f(1)f(9).$$

Here the relations  $A_1, A_2, A_3, B_1, B_2, B_3$  are given as

$$A_1 = \frac{\mu_f}{\mu_{hnf}}, A_2 = \frac{\rho_{hnf}}{\rho_f}, A_3 = \frac{\beta_{hnf}}{\beta_f}, B_1 = \frac{(\rho C_p)_{hnf}}{(\rho C_p)_f}, B_2 = \frac{k_{hnf}}{k_f}, B_3 = \frac{D_f}{D_{hnf}}.$$

This set of BVP problems is then solved by implementing Bvp4c code in MATLAB, along with the identified boundary conditions. The “inbuilt MATLAB code bvp4c” implements the three-stage Lobatto IIIa method [47], [38], [27].

## 5. Results and Analyses

An efficient numeric technique using the bvp4c code in MATLAB was employed to address the coupled formulation of the problem. At infinity, the boundary conditions are replaced by a suitable value  $\eta_{max}$ . The criteria for convergence are chosen to be accurate to six decimal places, and the step size is set to  $\Delta\eta = 0.001$ . The physical quantities of attention for the base fluid were computed at a value of  $\lambda = 0.5$  to determine the accurateness of the results. Compared to previously published studies, we discovered that they were in good agreement, as indicated in Table 2. As a result, it can be argued that the current code may be used to investigate the issue discussed in this study confidently. The impact of several factors, such as radiation constraint

**Table 2.** Numerical values of  $\frac{\mu_{hnf}}{\mu_{nf}} \left(1 + \frac{1}{\beta}\right) F''(0)$ ,  $\frac{\mu_{hnf}}{\mu_{nf}} \left(1 + \frac{1}{\beta}\right) G'(0)$  for different values of the rotational parameter ( $\omega$ ) and Casson parameter  $\beta$  and the base fluid, i.e.,  $\phi_1 = \phi_2 = Ri = Rd = Sc = \delta = S = 0$ ,  $\lambda = 1$

| Parameters |         | Butt <i>et al.</i> [5] |                     | Present study       |                     |
|------------|---------|------------------------|---------------------|---------------------|---------------------|
| $\lambda$  | $\beta$ | $C_{fx} Re_x^{1/2}$    | $Re_x^{1/2} C_{fy}$ | $C_{fx} Re_x^{1/2}$ | $Re_x^{1/2} C_{fy}$ |
| 0.5        | 2.0     | -1.394220              | -0.628002           | -1.394218           | -0.6280019          |
| 1.0        |         | -1.622822              | -1.025232           | -1.622817           | -1.0252172          |
| 5.0        |         | -2.92731               | -2.633846           | -2.927302           | -2.6338391          |
| 10.0       |         | -4.00746               | -3.797251           | -4.007467           | -3.7972510          |
| 0.5        | 2.0     | -1.39422               | -0.628002           | -4.007472           | -0.6280019          |
|            | 5.0     | -1.24703               | -0.561702           | -1.247049           | -0.5617016          |
|            | 10      | -1.19394               | -0.533778           | -1.193964           | -0.5337769          |
|            | 20      | -1.16649               | -0.525423           | -1.166489           | -0.5254322          |

( $0 \leq Rd < 3$ ), the Richardson number ( $0 \leq Ri \leq 6$ ), Schmidt number ( $0 \leq Sc < 3$ ), rotational parameter ( $0 \leq \omega < 3$ ), suction ( $0 \leq S < 3$ ), stretching parameter ( $0 \leq \lambda < 3$ ) (these values have been considered from the literature reviewed). The velocity, thermal, and mass diffusion fields were analysed and presented graphically.

The key purpose of the current segment is to explain the numerical outcomes for velocity, thermal, and mass diffusion profiles for a range of values of the physical constraints arising from the problem. Numerical values of local Nusselt, friction factor coefficients and Sherwood number are presented in tabular forms.

(a) Variation of Primary velocity gradient (PVG) and Secondary velocity Gradient (SVG) with different parameters:

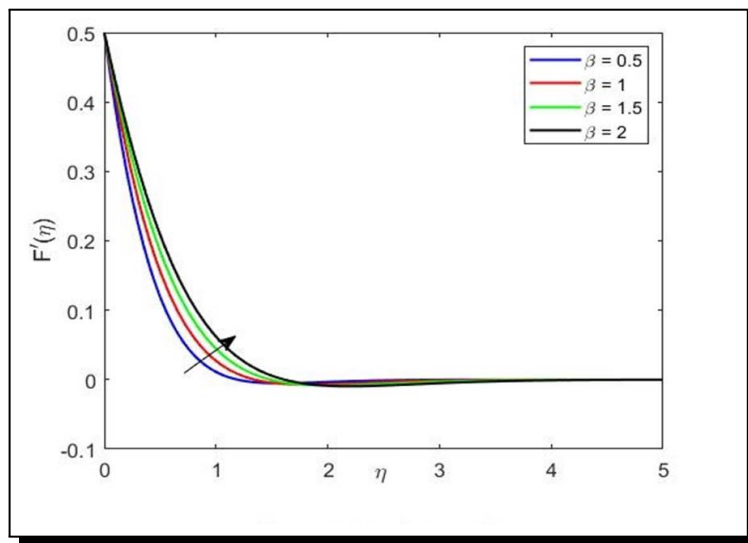


**Figure 2.** Variation of  $F'(\eta)$  with  $\beta$

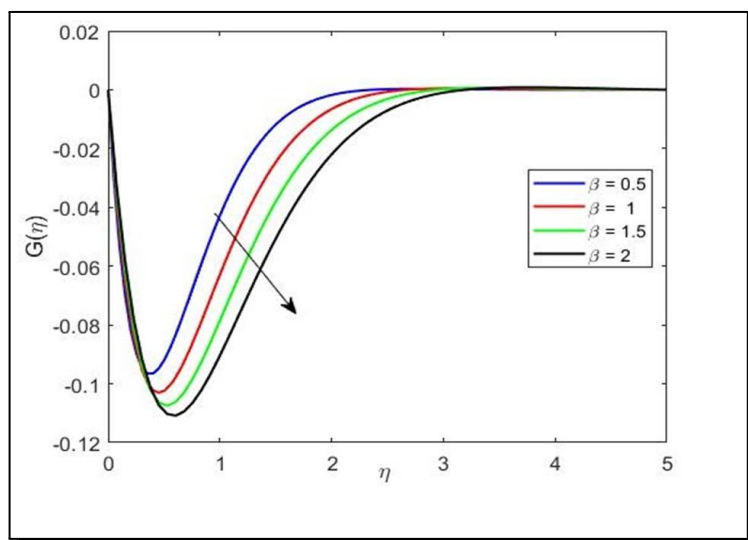


**Figure 3.** Variation of  $G(\eta)$  with  $\beta$

Figure 2 and Figure 3 illustrate the effect of the Casson parameter  $\beta$  on the primary and secondary velocities. From the figures, we can infer that as the value of  $\beta$  improves, the primary velocity increases, whereas the secondary velocity decreases.

The impact of the source parameter  $\delta$  on the PVG and SVG can be noticed in Figure 4 and Figure 5. The rise in the  $\delta$  values improves the PVG and negatively impacts SVG because the source parameter increases the velocity boundary layer.

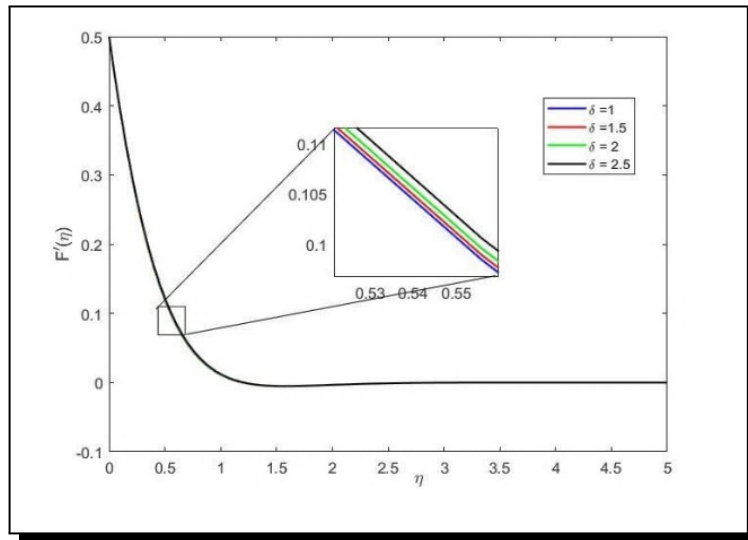


Figure 4. Influence of the Source parameter ( $\delta$ ) on  $F'(\eta)$

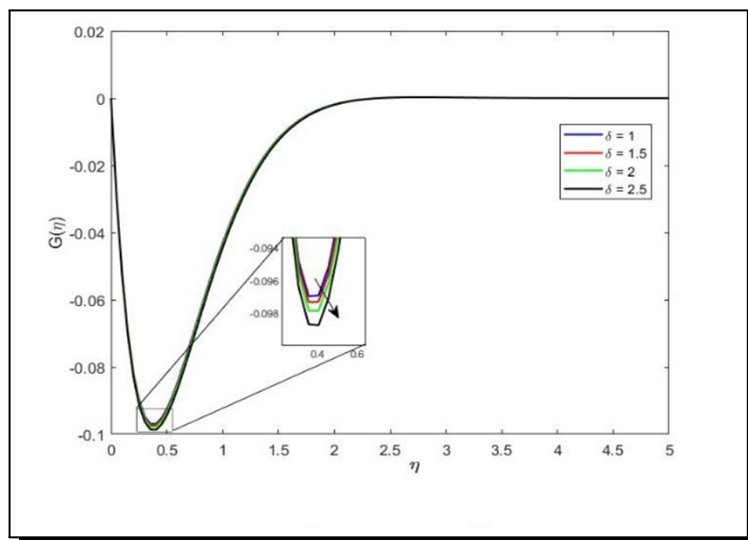


Figure 5. Influence of the Source parameter ( $\delta$ ) on  $G(\eta)$

Figure 6 and Figure 7 display the physical characteristic change in PVG and SVG. The growing values of the stretching parameter  $\lambda$  surge the primary boundary layer and deflate the SVG.

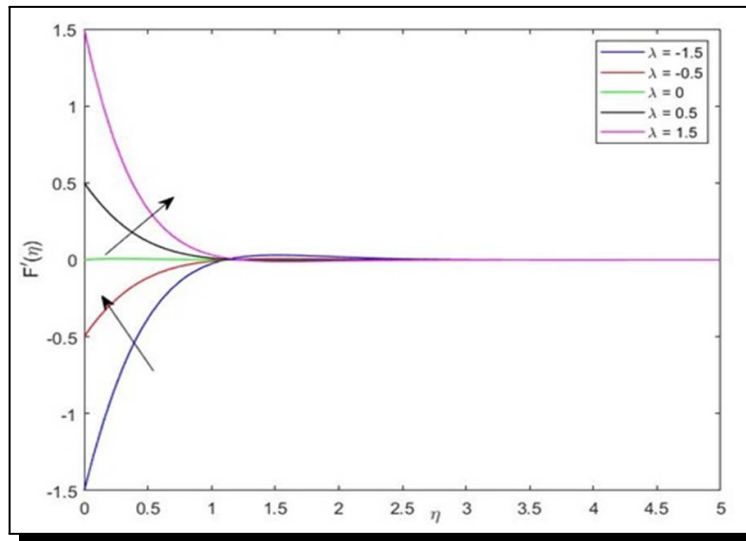


Figure 6. Effect of  $\lambda$  on  $F'(\eta)$

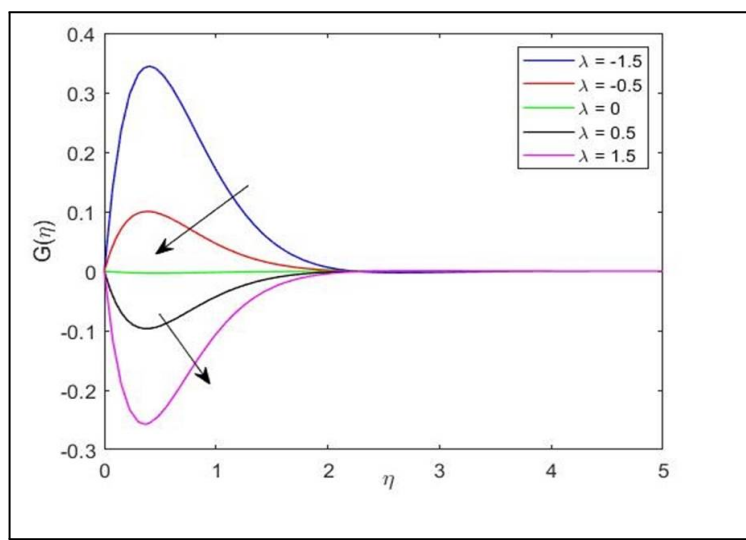


Figure 7. Effect of  $\lambda$  on  $G(\eta)$

Richardson number  $Ri$  is a convective boundary that can easily merge [32].  $Ri < 0$  has an opposing buoyance stream,  $Ri > 0$  has an assisting buoyance stream, and  $Ri = 0$  recovers the instance of an utterly limited convective stream without any lightness impacts. Thus Figure 8 and Figure 9 show that the improvement in the values of PVG with the rise in  $Ri$  and the opposite nature is found on SVG.

Figure 10 and Figure 11 represent the suction effect on PVG and SVG; as Suction is a boundary layer control strategy, it reduces drag on bodies in an external flow or channel energy loss. Thus, these figures demonstrate that primary velocity reduces dramatically as the suction parameter increases and the secondary velocity rises.

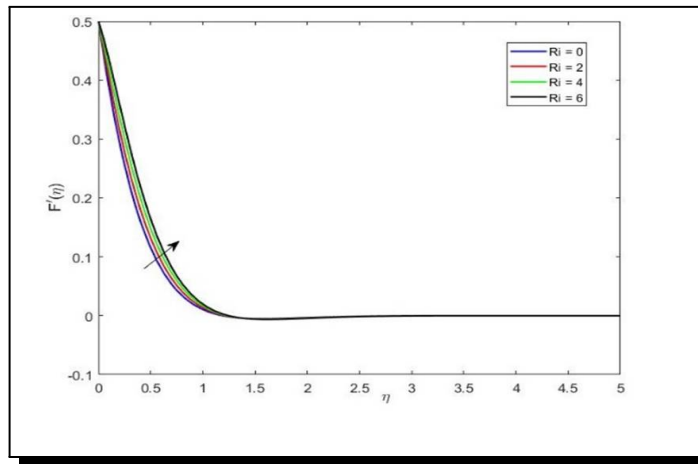


Figure 8. Effect of  $Ri$  on  $F'(\eta)$

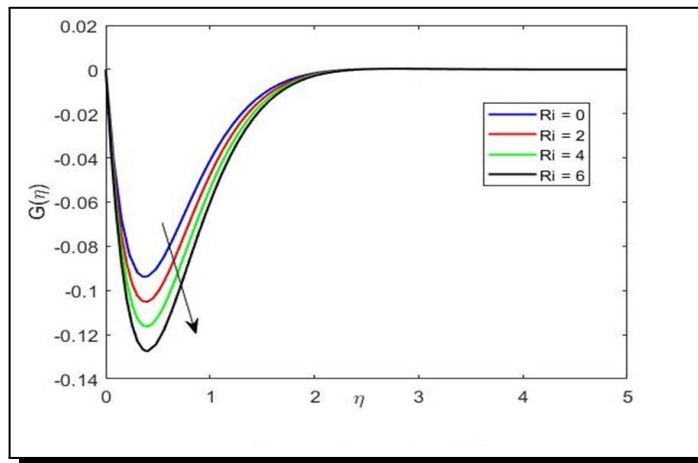


Figure 9. Effect of  $Ri$  on  $G(\eta)$

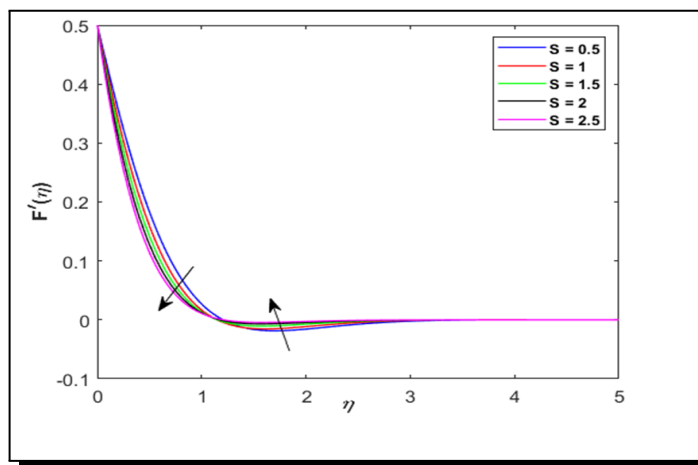
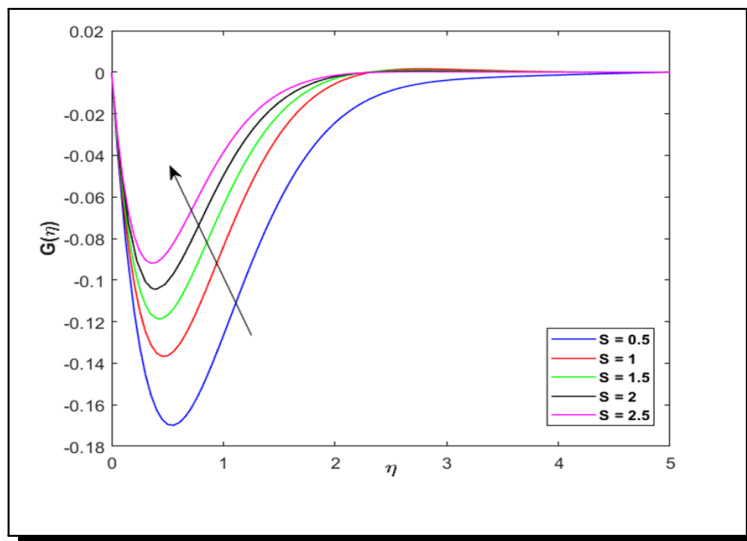
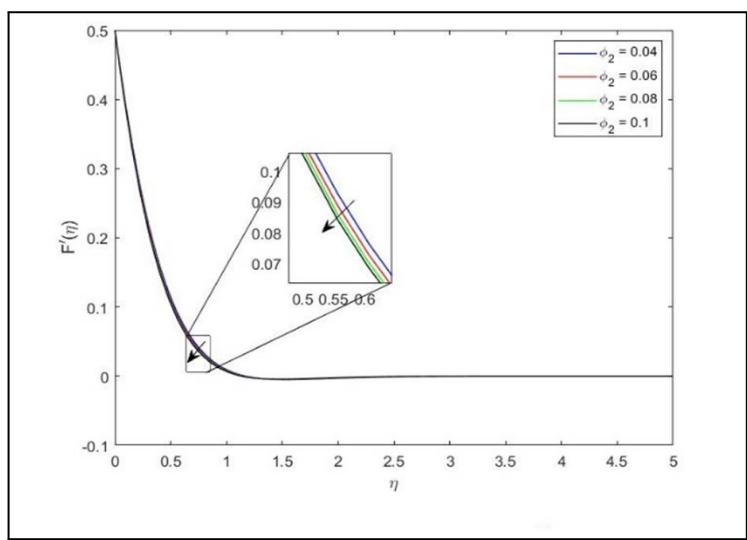


Figure 10. Effect of  $S$  on  $F'(\eta)$



**Figure 11.** Effect of  $S$  on  $G(\eta)$



**Figure 12.** Influence of the Cu nanoparticle volume fraction  $\phi_2$  on  $F'(\eta)$

It is illustrated in Figure 12 and Figure 13, that enhancing the volume fraction accelerates both primary and secondary flow in the HNF owing to increased interaction between the suspended nanoparticles.

The variation of primary and secondary velocity distribution with the rise in the radiation parameter value is portrayed in Figure 14 to Figure 17 show that the Coriolis force is predominant in the fluid medium along the spinning path. It is believed that the velocity components decrease when the rotation parameter increases.

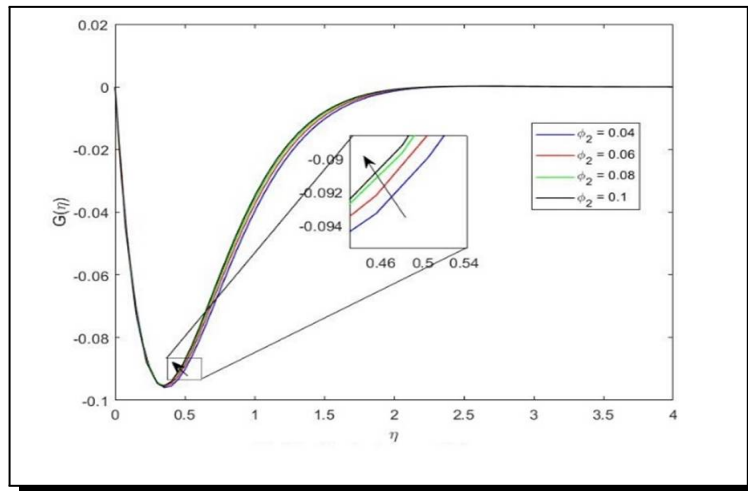


Figure 13. Influence of the Cu nanoparticle volume fraction  $\phi_2$  on  $G(\eta)$

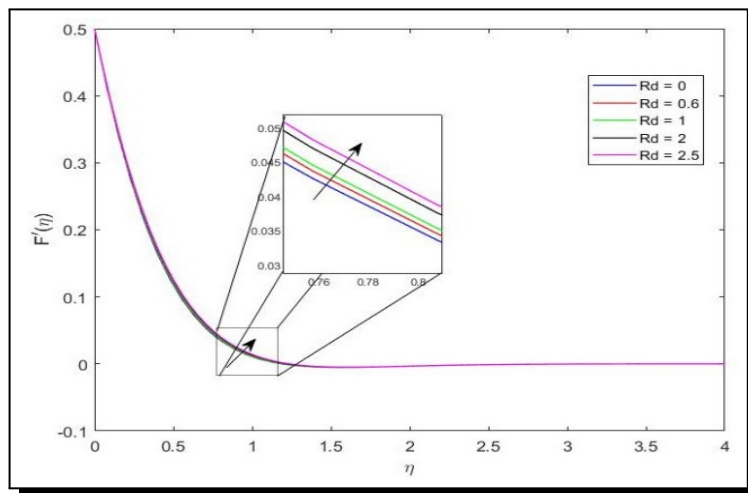


Figure 14. Effect of  $Rd$  on  $F'(\eta)$

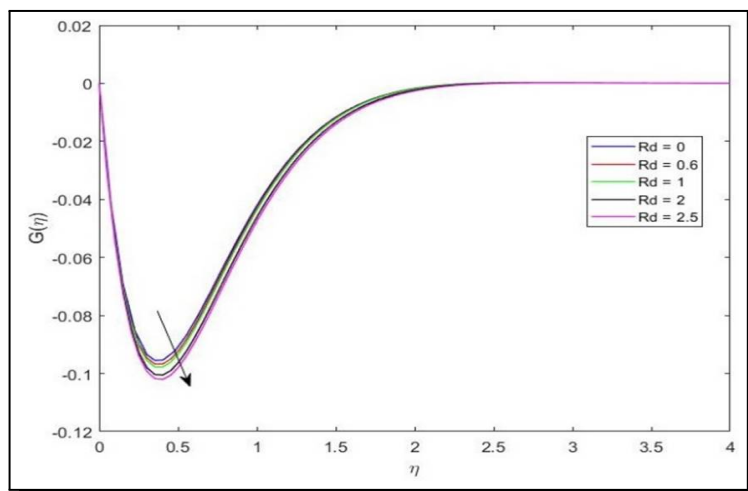
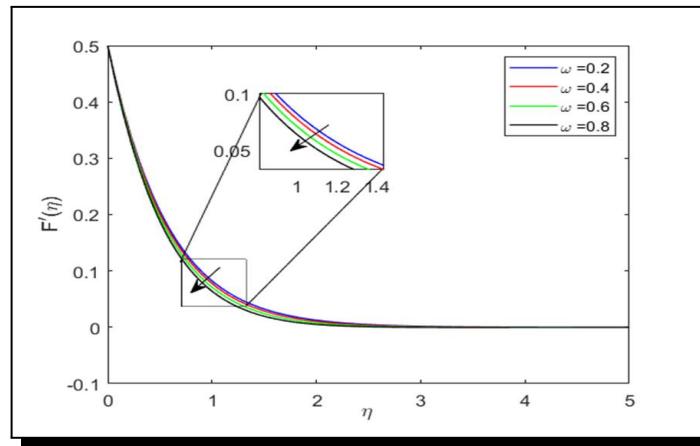
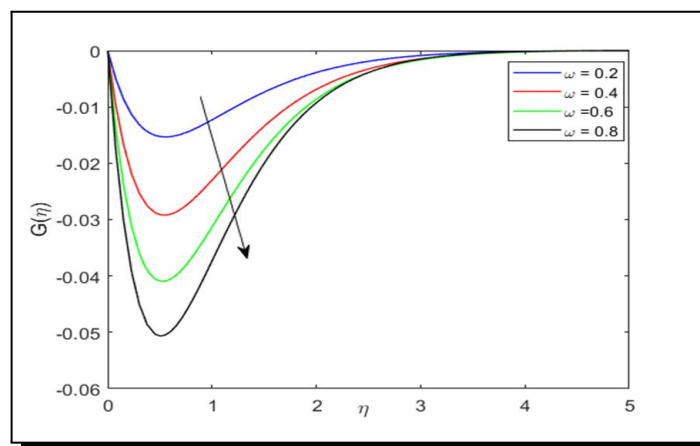


Figure 15. Effect of  $Rd$  on  $G(\eta)$



**Figure 16.** Influence of rotation parameter ( $\omega$ ) on  $F'(\eta)$



**Figure 17.** Influence of rotation parameter ( $\omega$ ) on  $G(\eta)$

(b) The behaviour of thermal and concentration boundary layers (TBL & CBL) with various parameters:

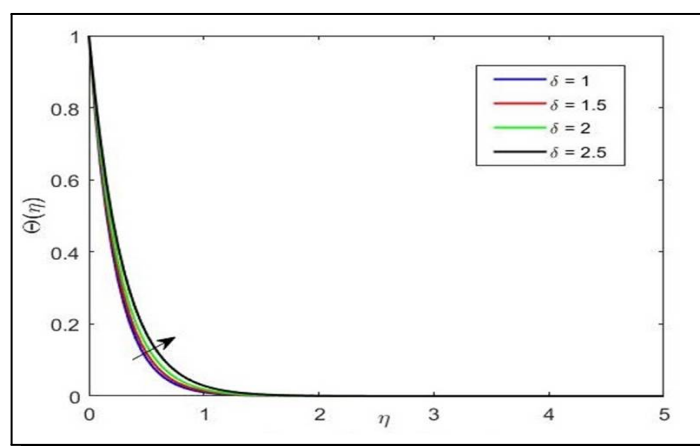


**Figure 18.** Behaviour of  $\Theta(\eta)$  with variation in  $\delta$

The TBL increases in the existence of a heat source which leads to the improvement of the temperature profile of the HNF flow. This can be observed in Figure 18. The impact of the stretching parameter  $\lambda$  can be seen in Figure 19 and Figure 20. They demonstrate that as the values of  $\lambda$  surge, the TBL and CBL decrease, resulting in a fall in temperature and mass diffusion.

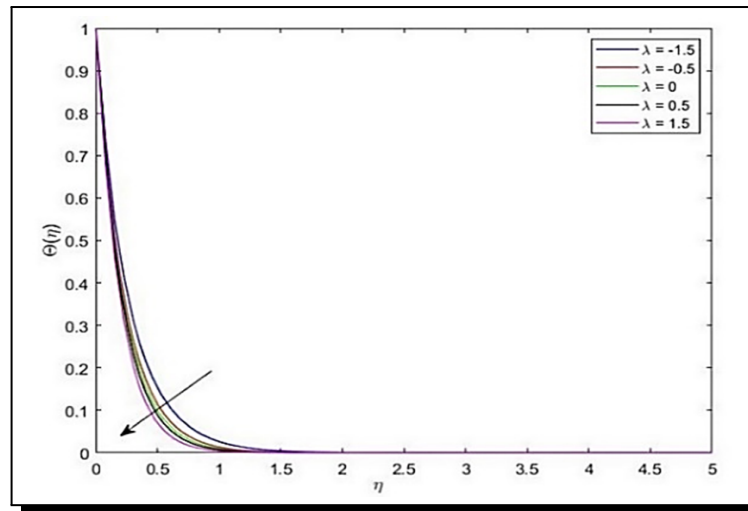


**Figure 19.** Behaviour of  $\Theta(\eta)$  with variation in  $\lambda$

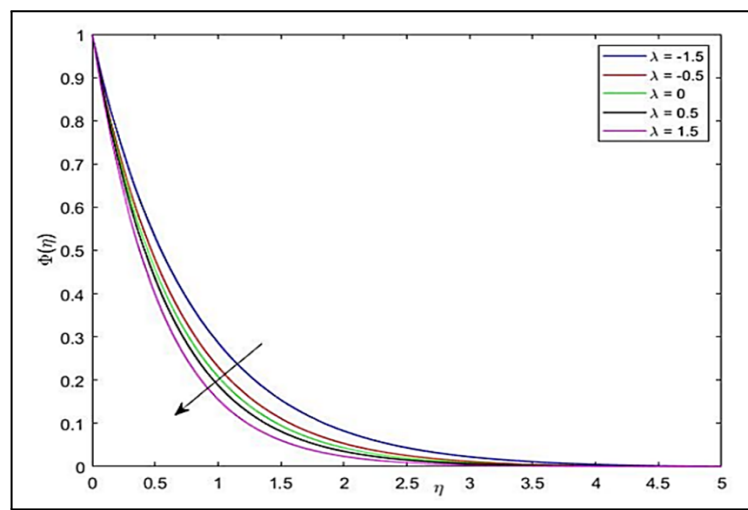


**Figure 20.** Behaviour of  $\Phi(\eta)$  with variation in  $\lambda$

Figure 21 and Figure 22 depict the behaviour of the TBL and CBL with the variation in the values of the suction parameter. As the values of  $S$  excavate, both TBL and CBL decrease because the suction reduces the BLT (boundary layer thickness). From Figure 23 and Figure 25, we notice that the rise in the Cu solid nanoparticle volume fraction leads to an improvement in the temperature field and a fall in the mass diffusion.

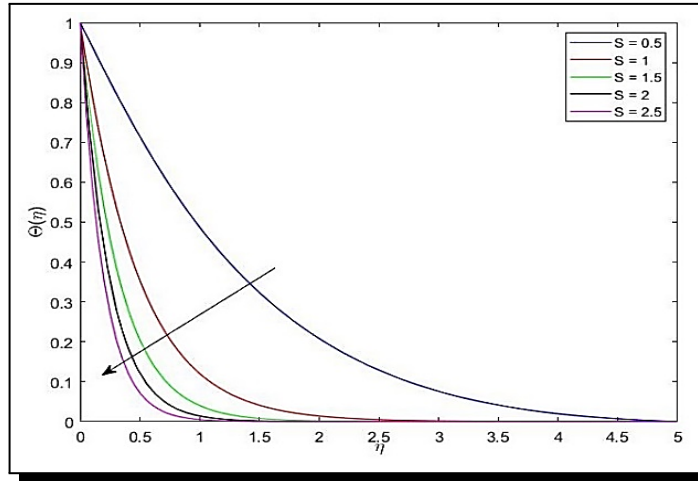


Figure 21. Behaviour of  $\Theta(\eta)$  with Suction ( $S$ )

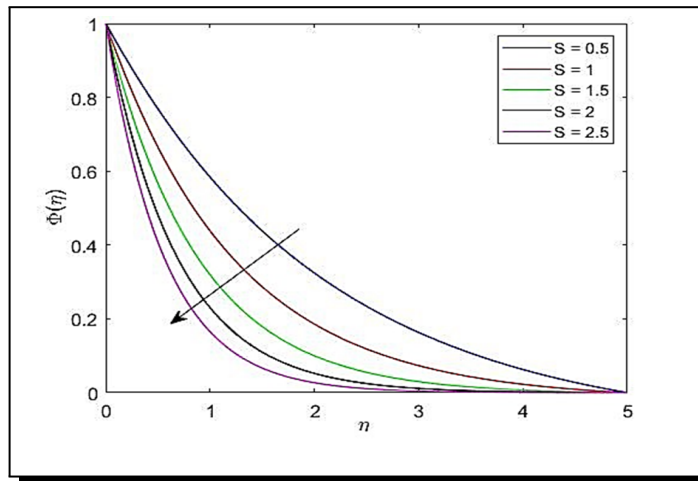


Figure 22. Behaviour of  $\Phi(\eta)$  with change in  $S$

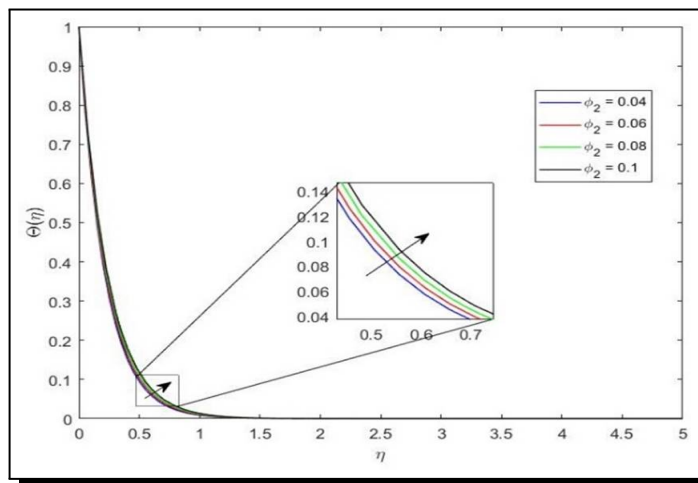


Figure 23. Effect of  $\phi_2$  on  $\Theta(\eta)$

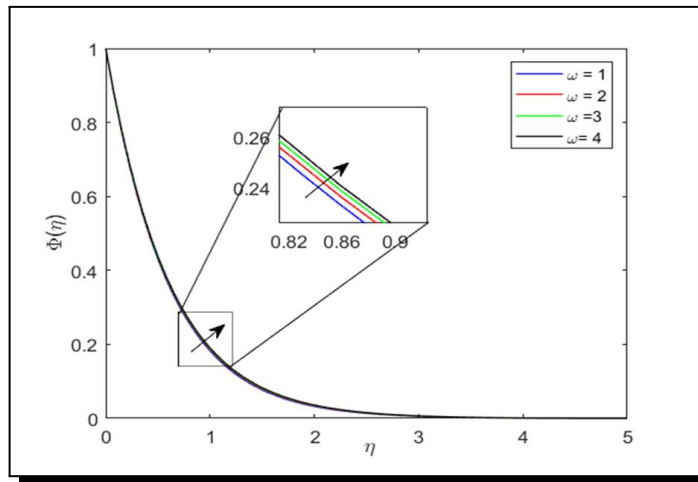


Figure 24. Effect of the rotational parameter ( $\omega$ ) on  $\Phi(\eta)$

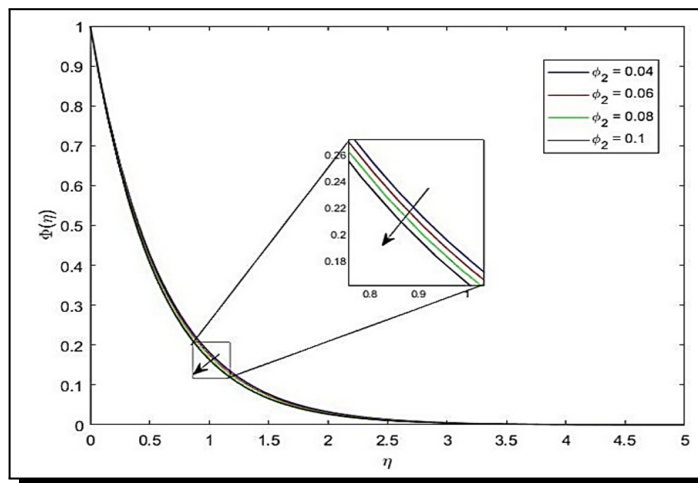


Figure 25. Effect of  $\phi_2$  on  $\Phi(\eta)$

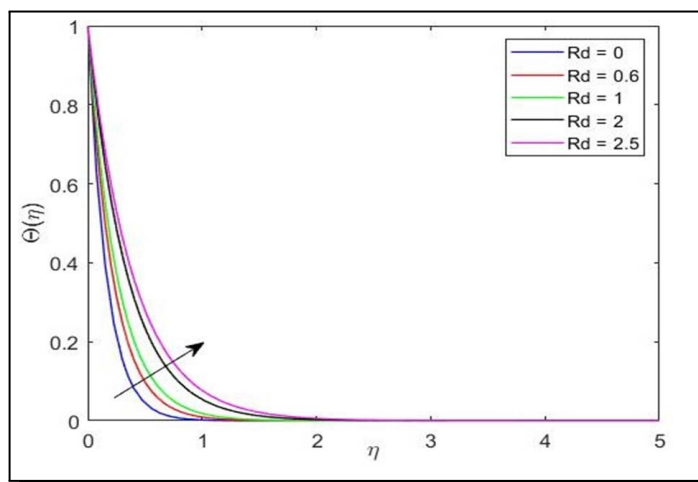
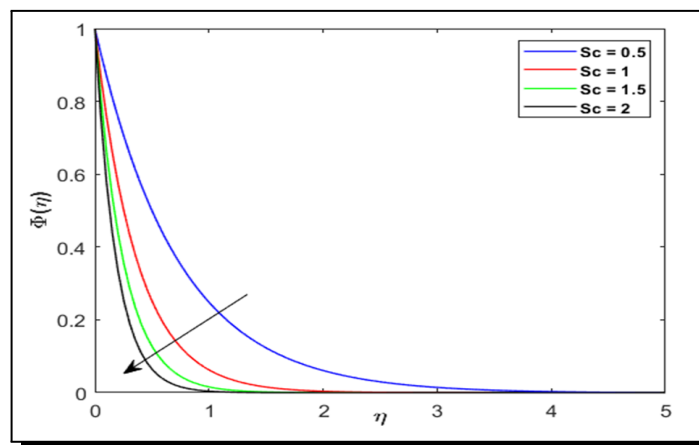


Figure 26. Influence of  $Rd$  on  $\Theta(\eta)$



**Figure 27.** Influence of  $Sc$  on  $\Phi(\eta)$

The improvement of the rotational parameter values leads to surge of the CBL, which can be observed from the Figure 24.

Figure 26 divulges that the rise in the radiation parameter elevates the TBL resulting. Physically, the increased thermal energy released in the boundary layer is owing to the thermal radiation parameter's highest values. As a result, the thermal boundary layers that correspond to them are thicker. These findings apply to a wide variety of real-world engineering applications that require maximal heat transmission.

The concentration gradient deteriorates as the value of  $Sc$  rises (Figure 27).  $Sc$  is a dimensionless quantity in a fluid flow that explains the connection between momentum and mass diffusivity. The smallest  $Sc$  correlates to the highest nanoparticle concentration. The width of the hydrodynamic and nanoparticle composition boundary layers is also shown. Mass diffusion, which occurs as a result of an elevation in the  $Sc$ , causes the concentration gradient to decay.

Table 3 elucidates the calculated values of the physical parameter of technical interest. This table shows that the improvement in the rotational parameter ( $\omega$ ) values lead to the decrement of all the physical parameters. The "heat and mass transfer rate coefficients" surge when the values of  $\phi_2$ ,  $\beta$ ,  $Rd$ ,  $Ri$ ,  $S$ ,  $\delta$  rise, while the reverse behaviour is observed in the primary and secondary skin friction values.

## 6. Conclusions

The convective Casson flow across a revolving stretching sheet with suction and thermal radiation was investigated in this study. The following are the key findings of the present investigation:

- (i) The increase in suction, heat source and radiation improve the temperature and the concentration profiles.
- (ii) The improved values of the Richardson parameter result in a rise in the primary velocity profile and a decline in the secondary velocity profile.

**Table 3.** Calculated physical parameter values, i.e., “local skin frictions in x, y direction, local Nusselt number, local Sherwood number”

| $\omega$ | $\phi_2$ | $\beta$ | $\delta$ | $Rd$ | $Ri$ | $S$ | $C_{fx}Re_x^{1/2}$ | $Re_x^{1/2}C_{fy}$ | $Nu_xRe_x^{-1/2}$ | $Re_x^{-1/2}Sh_x$ |
|----------|----------|---------|----------|------|------|-----|--------------------|--------------------|-------------------|-------------------|
| 0.01     | 0.02     | 1.5     | 0.5      | 0.5  | 1    | 2.3 | -1.881033          | -0.027094          | 0.937795          | 2.127673          |
| 0.02     |          |         |          |      |      |     | -1.881230          | -0.054236          | 0.937742          | 2.127660          |
| 0.04     |          |         |          |      |      |     | -1.882020          | -0.108420          | 0.937543          | 2.127605          |
| 0.06     |          |         |          |      |      |     | -1.883334          | -0.162498          | 0.937215          | 2.127513          |
|          | 0.01     |         |          |      |      |     | -2.406684          | -0.895419          | 10.711826         | 2.014740          |
|          | 0.02     |         |          |      |      |     | -2.395549          | -0.927544          | 10.763866         | 2.092348          |
|          | 0.03     |         |          |      |      |     | -2.378378          | -0.960020          | 10.815323         | 2.172875          |
|          | 0.04     |         |          |      |      |     | -2.355663          | -0.992980          | 10.866232         | 2.256452          |
|          |          | 0.5     |          |      |      |     | -2.279095          | -0.796379          | 10.740209         | 2.072778          |
|          |          | 1       |          |      |      |     | -2.504733          | -1.046024          | 10.780704         | 2.107249          |
|          |          | 1.5     |          |      |      |     | -2.705417          | -1.255521          | 10.803287         | 2.128562          |
|          |          | 2       |          |      |      |     | -2.887475          | -1.438975          | 10.817916         | 2.143187          |
|          |          |         | 0.5      |      |      |     | -2.395549          | -0.927544          | 9.311177          | 2.092348          |
|          |          |         | 1        |      |      |     | -2.393243          | -0.927870          | 9.840525          | 2.092422          |
|          |          |         | 1.5      |      |      |     | -2.390567          | -0.928262          | 10.321108         | 2.092511          |
|          |          |         | 2        |      |      |     | -2.387391          | -0.928745          | 10.763866         | 2.092618          |
|          |          |         |          | 0.5  |      |     | -2.395549          | -0.927544          | 10.763866         | 2.092348          |
|          |          |         |          | 1    |      |     | -2.383114          | -0.929526          | 11.718042         | 2.092783          |
|          |          |         |          | 1.5  |      |     | -2.371042          | -0.931836          | 12.383008         | 2.093258          |
|          |          |         |          | 2    |      |     | -2.359274          | -0.934474          | 12.869527         | 2.093768          |
|          |          |         |          |      | 0.5  |     | -2.395549          | -0.927544          | 10.763866         | 2.092348          |
|          |          |         |          |      | 1    |     | -2.330489          | -0.932037          | 10.765949         | 2.093492          |
|          |          |         |          |      | 1.5  |     | -2.265496          | -0.936508          | 10.768025         | 2.094631          |
|          |          |         |          |      | 2    |     | -2.200568          | -0.940957          | 10.770096         | 2.095767          |
|          |          |         |          |      |      | 0.5 | -1.401146          | -1.153617          | 2.784717          | 0.887125          |
|          |          |         |          |      |      | 1   | -1.664265          | -1.101065          | 4.971288          | 1.198562          |
|          |          |         |          |      |      | 1.5 | -1.933955          | -1.039598          | 7.184205          | 1.531428          |
|          |          |         |          |      |      | 2   | -2.217693          | -0.970611          | 9.417196          | 1.878765          |

(iii) The surge in the  $Ri$  value also improves the skin friction, the mass and heat rate coefficients.

(iv) The rise in  $Sc$  declines the concentration profile.

(v) For larger  $\beta$  values, skin friction measure, “transverse skin friction coefficient”, are condensed, whereas the “local Nusselt and Sherwood numbers” values are inflated.

Although opposite performance for opposing flow ( $\lambda < 0$ ) is seen, the skin friction coefficient declines for aiding flow ( $\lambda > 0$ ).

## Competing Interests

The authors declare that they have no competing interests.

## Authors' Contributions

All the authors contributed significantly in writing this article. The authors read and approved the final manuscript.

## References

- [1] Z. A. Alhussain and A. Tassaddiq, Thin film blood based Casson hybrid nanofluid flow with variable viscosity, *Arabian Journal for Science and Engineering* **47**(1) (2022), 1087 – 1094, DOI: 10.1007/s13369-021-06067-8.
- [2] B. Ali, R. A. Naqvi, D. Hussain, O. M. Aldossary and S. Hussain, Magnetic rotating flow of a hybrid nano-materials ag MoS<sub>2</sub> and Go MoS<sub>2</sub> in C<sub>2</sub>H<sub>6</sub>O<sub>2</sub> H<sub>2</sub>O hybrid base fluid over an extending surface involving activation energy: Fe simulation, *Mathematics* **8**(10) (2020), 1730, DOI: 10.3390/math8101730.
- [3] N. S. Anuar, N. Bachok and I. Pop, Radiative hybrid nanofluid flow past a rotating permeable stretching/shrinking sheet, *International Journal of Numerical Methods for Heat & Fluid Flow* **31**(3) (2020), 914 – 932, DOI: 10.1108/HFF-03-2020-0149.
- [4] M. Archana, B. J. Gireesha, B. C. Prasannakumara and R. S. R. Gorla, Influence of nonlinear thermal radiation on rotating flow of Casson nanofluid, *Nonlinear Engineering* **7**(2) (2018), 91 – 101, DOI: 10.1515/nleng-2017-0041.
- [5] A. S. Butt, A. Ali and A. Mehmood, Study of flow and heat transfer on a stretching surface in a rotating Casson fluid, *Proceedings of the National Academy of Sciences, India Section A: Physical Sciences* **85**(3) (2015), 421 – 426, DOI: 10.1007/s40010-015-0217-1.
- [6] N. Casson, A flow equation for pigment-oil suspensions of the printing ink type, in: *Rheology of Disperse Systems*, C. C. Mill (ed.), Pergamon Press, Oxford, 84 – 104 (1959).
- [7] K. M. Chandrashekar, M. M. Nandeppanavar, R. Nagaraj and S. Madikiri, Effects of Richardson and Biot number on double-diffusive Casson fluid flow with viscous dissipation, *Heat Transfer* **51**(2) (2022), 2003 – 2019, DOI: 10.1002/htj.22385.
- [8] B. Devaki, N. P. Pai and K. V. S. Sampath, Analysis of MHD flow and heat transfer of Casson fluid flow between porous disks, *Journal of Advanced Research in Fluid Mechanics and Thermal Sciences* **83**(1) (2021), 46 – 60, DOI: 10.37934/arfmts.83.1.4660.
- [9] S. S. U. Devi and S. P. A. Devi, Numerical investigation of three-dimensional hybrid Cu-Al<sub>2</sub>O<sub>3</sub>/water nanofluid flow over a stretching sheet with effecting Lorentz force subject to Newtonian heating, *Canadian Journal of Physics* **94**(5) (2016), 490 – 496, DOI: 10.1139/cjp-2015-0799.
- [10] R. Ellahi, Special issue on recent developments of nanofluids, *Applied Sciences* **8**(2) (2018), 192, DOI: 10.3390/app8020192.
- [11] E. R. EL-Zahar, A. M. Rashad, W. Saad and L. F. Seddek, Magneto-hybrid nanofluids flow via mixed convection past a radiative circular cylinder, *Scientific Reports* **10** (2020), Article number: 10494, DOI: 10.1038/s41598-020-66918-6.

- [12] B. J. Gireesha, G. Sowmya, M. I. Khan and H. F. Öztöp, Flow of hybrid nanofluid across a permeable longitudinal moving fin along with thermal radiation and natural convection, *Computer Methods and Programs in Biomedicine* **185** (2020), 105166, DOI: 10.1016/j.cmpb.2019.105166.
- [13] T. Gul, M. Bilal, M. Shuaib, S. Mukhtar and P. Thounthong, Thin film flow of the water-based carbon nanotubes hybrid nanofluid under the magnetic effects, *Heat Transfer* **49**(6) (2020), 3211 – 3227, DOI: 10.1002/HTJ.21770.
- [14] T. Hayat and S. Nadeem, An improvement in heat transfer for rotating flow of hybrid nanofluid: A numerical study, *Canadian Journal of Physics* **96**(12) (2018), 1420 – 1430, DOI: 10.1139/cjp-2017-0801.
- [15] T. Hayat and S. Nadeem, Heat transfer enhancement with Ag-CuO/water hybrid nanofluid, *Results in Physics* **7** (2017), 2317 – 2324, DOI: 10.1016/j.rinp.2017.06.034.
- [16] T. Hayat, S. Nadeem and A. U. Khan, Rotating flow of Ag-CuO/H<sub>2</sub>O hybrid nanofluid with radiation and partial slip boundary effects, *The European Physical Journal E* **41** (2018), Article number: 75, DOI: 10.1140/EPJE/I2018-11682-Y.
- [17] A. Hussain, Q. Haider, A. Rehman, H. Ahmad, J. Baili, N. H. Aljahdaly and A. Hassan, A thermal conductivity model for hybrid heat and mass transfer investigation of single and multi-wall carbon nano-tubes flow induced by a spinning body, *Case Studies in Thermal Engineering* **28** (2021), 101449, DOI: 10.1016/j.csite.2021.101449.
- [18] W. Ibrahim and O. D. Makinde, Magnetohydrodynamic stagnation point flow and heat transfer of casson nanofluid past a stretching sheet with slip and convective boundary condition, *Journal of Aerospace Engineering* **29**(2) (2016), 04015037, DOI: 10.1061/(asce)as.1943-5525.0000529.
- [19] N. Iftikhar, A. Rehman, H. Sadaf and S. Iqbal, Study of Al<sub>2</sub>O<sub>3</sub>/copper-water nanoparticle shape, slip effects, and heat transfer on steady physiological delivery of MHD hybrid nanofluid, *Canadian Journal of Physics* **97**(12) (2019), 1239 – 1252, DOI: 10.1139/cjp-2018-0551.
- [20] W. Jamshed and A. Aziz, A comparative entropy based analysis of Cu and Fe<sub>3</sub>O<sub>4</sub>/methanol Powell-Eyring nanofluid in solar thermal collectors subjected to thermal radiation, variable thermal conductivity and impact of different nanoparticles shape, *Results in Physics* **9** (2018), 195 – 205, DOI: 10.1016/j.rinp.2018.01.063.
- [21] W. Jamshed, S. S. U. Devi, M. Goodarzi, M. Prakash, K. S. Nisar, M. Zakarya and A.-H. Abdel-Aty, Evaluating the unsteady Casson nanofluid over a stretching sheet with solar thermal radiation: An optimal case study, *Case Studies in Thermal Engineering* **26** (2021), 101160, DOI: 10.1016/j.csite.2021.101160.
- [22] S. Khan, M. M. Selim, A. Khan, A. Ullah, T. Abdeljawad, Ikramullah, M. Ayaz and W. K. Mashwani, On the analysis of the non-newtonian fluid flow past a stretching/shrinking permeable surface with heat and mass transfer, *Coatings* **11**(5) (2021), 566, DOI: 10.3390/coatings11050566.
- [23] M. I. Khan, M. Waqas, T. Hayat and A. Alsaedi, A comparative study of Casson fluid with homogeneous-heterogeneous reactions, *Journal of Colloid and Interface Science* **498** (2017), 85 – 90, DOI: 10.1016/j.jcis.2017.03.024.

- [24] M. Khan, T. Salahuddin, M. M. Yousaf, F. Khan and A. Hussain, Variable diffusion and conductivity change in 3D rotating Williamson fluid flow along with magnetic field and activation energy Magnetic field and activation energy, *International Journal of Numerical Methods for Heat & Fluid Flow* **30**(5) (2022), 2467 – 2484, DOI: 10.1108/HFF-02-2019-0145.
- [25] Y. H. Krishna, G. V. R. Reddy and O. D. Makinde, Chemical reaction effect on MHD flow of Casson fluid with porous stretching sheet, *Defect and Diffusion Forum* **389** (2018), 100 – 109, DOI: 10.4028/www.scientific.net/DDF.389.100.
- [26] M. V. Krishna, N. A. Ahammad and A. J. Chamkha, Radiative MHD flow of Casson hybrid nanofluid over an infinite exponentially accelerated vertical porous surface, *Case Studies in Thermal Engineering* **27** (2021), 101229, DOI: 10.1016/j.csite.2021.101229.
- [27] L. A. Lund, Z. Omar, I. Khan and E. S. M. Sherif, Dual branches of MHD three-dimensional rotating flow of hybrid nanofluid on nonlinear shrinking sheet, *Computers, Materials & Continua* **66**(1) (2021), 127 – 139, DOI: 10.32604/cmc.2020.013120.
- [28] L. A. Lund, Z. Omar, J. Raza and I. Khan, Magnetohydrodynamic flow of Cu-Fe<sub>3</sub>O<sub>4</sub>/H<sub>2</sub>O hybrid nanofluid with effect of viscous dissipation: Dual similarity solutions, *Journal of Thermal Analysis and Calorimetry* **143**(2) (2021), 915 – 927, DOI: 10.1007/S10973-020-09602-1.
- [29] A. Mahdy and A. Chamkha, Heat transfer and fluid flow of a non-Newtonian nanofluid over an unsteady contracting cylinder employing Buongiorno's model, *International Journal of Numerical Methods for Heat & Fluid Flow* **25**(4) (2015), 703 – 723, DOI: 10.1108/HFF-04-2014-0093.
- [30] M. K. Murthy, C. S. K. Raju, V. Nagendramma, S. A. Shehzad and A. J. Chamkha, Magnetohydrodynamics boundary layer slip Casson fluid flow over a dissipated stretched cylinder, *Defect and Diffusion Forum* **393** (2019), 73 – 82, DOI: 10.4028/www.scientific.net/DDF.393.73.
- [31] M. M. Nandeppanavar, M. C. Kemparaju and N. Raveendra, Double-diffusive free convective flow of Casson fluid due to a moving vertical plate with non-linear thermal radiation, *World Journal of Engineering* **18**(1) (2021), 85 – 93, DOI: 10.1108/WJE-06-2020-0215.
- [32] M. M. Nandeppanavar, M. C. Kemparaju and R. Nagaraj, Effect of Richardson number on stagnation point flow of double diffusive mixed convective slip flow of MHD Casson fluid: A numerical study, *Computational and Mathematical Methods* **3**(6) (2021), e1209, DOI: 10.1002/cmm4.1209.
- [33] K. S. Nisar, U. Khan, A. Zaib, I. Khan and D. Baleanu, Exploration of aluminum and titanium alloys in the stream-wise and secondary flow directions comprising the significant impacts of magnetohydrodynamic and hybrid nanofluid, *Crystals* **10** (2020), 679, DOI: 10.3390/cryst10080679.
- [34] H. A. Ogunseye, Y. O. Tijani and P. Sibanda, Entropy generation in an unsteady Eyring-Powell hybrid nanofluid flow over a permeable surface: A Lie group analysis, *Heat Transfer* **49**(6) (2020), 3374 – 3390, DOI: 10.1002/HTJ.21778.
- [35] A. S. Oke, W. N. Mutuku, M. Kimathi and I. L. Animasaun, Insight into the dynamics of non-Newtonian Casson fluid over a rotating non-uniform surface subject to Coriolis force, *Nonlinear Engineering* **9**(1) (2020), 398 – 411, DOI: 10.1515/nleng-2020-0025.
- [36] W. Owhaib, M. Basavarajappa and W. Al-Kouz, Radiation effects on 3D rotating flow of Cu-water nanoliquid with viscous heating and prescribed heat flux using modified Buongiorno model, *Scientific Reports* **11** (2021), Article number: 20669, DOI: 10.1038/s41598-021-00107-x.

- [37] K. Pietrak and T. Wiśniewski, A review of models for effective thermal conductivity of composite materials, *Journal of Power Technologies* **95**(1) (2015), 14 – 24, <https://papers.itc.pw.edu.pl/index.php/JPT/article/view/463>.
- [38] S. G. Pinto, S. P. Rodríguez and J. I. M. Torcal, On the numerical solution of stiff IVPs by Lobatto IIIA Runge-Kutta methods, *Journal of Computational and Applied Mathematics* **82**(1-2) (1997), 129 – 148, DOI: 10.1016/s0377-0427(97)00086-1.
- [39] P. D. Prasad, S. V. K. Varma, C. S. K. Raju, S. A. Shehzad and M. A. Meraj, 3D flow of Carreau polymer fluid over variable thickness sheet in a suspension of microorganisms with Cattaneo-Christov heat flux, *Revista Mexicana de Física* **64**(5) (2018), 519 – 529, DOI: 10.31349/revmexfis.64.519.
- [40] A. Prathiba and V. L. Akavaram, Numerical investigation of a convective hybrid nanofluids around a rotating sheet, *Heat Transfer* **51**(4) (2022). 3353 – 3372 DOI: 10.1002/htj.22454.
- [41] J. V. R. Reddy, V. Sugunamma and N. Sandeep, Impact of Soret and Dufour numbers on MHD Casson fluid flow past an exponentially stretching sheet with non-uniform heat source/sink, *Defect and Diffusion Forum* **388** (2018), 14 – 27, DOI: 10.4028/www.scientific.net/DDF.388.14.
- [42] A. Saeed, A. Alsubie, P. Kumam, S. Nasir, T. Gul and W. Kumam, Blood based hybrid nanofluid flow together with electromagnetic field and couple stresses, *Scientific Reports* **11** (2021), Article number: 12865, DOI: 10.1038/s41598-021-92186-z.
- [43] M. U. Sajid and H. M. Ali, Thermal conductivity of hybrid nanofluids: A critical review, *International Journal of Heat and Mass Transfer* **126** (2018), 211 – 234, DOI: 10.1016/j.ijheatmasstransfer.2018.05.021.
- [44] D. U. Sarwe, B. Shanker, R. Mishra, R. S. V. Kumar, M. N. R. Shekar, Simultaneous impact of magnetic and Arrhenius activation energy on the flow of Casson hybrid nanofluid over a vertically moving plate, *International Journal of Thermofluid Science and Technology* **8**(2) (2021), Paper number 080202, DOI: 10.36963/ijst.2021080202.
- [45] I. Y. Seini, G. Aloliga, B. Ziblim and O. D. Makinde, Boundary Layer flow of casson fluid on exponentially stretching porous surface with radiative heat transfer, *Diffusion Foundations* **26** (2020), 112 – 125, DOI: 10.4028/www.scientific.net/DF.26.112.
- [46] Z. Shah, E. Bonyah, S. Islam and T. Gul, Impact of thermal radiation on electrical MHD rotating flow of Carbon nanotubes over a stretching sheet, *AIP Advances* **9**(1) (2019), 015115, DOI: 10.1063/1.5048078.
- [47] M. Shoaib, M. A. Z. Raja, M. T. Sabir, M. Awais, S. Islam, Z. Shah and P. Kumam, Numerical analysis of 3-D MHD hybrid nanofluid over a rotational disk in presence of thermal radiation with Joule heating and viscous dissipation effects using Lobatto IIIA technique, *Alexandria Engineering Journal* **60**(4) (2021), 3605 – 3619, DOI: 10.1016/j.aej.2021.02.015.
- [48] A. Shojaei, A. J. Amiri, S. S. Ardahaie, K. Hosseinzadeh and D. D. Ganji, Hydrothermal analysis of Non-Newtonian second grade fluid flow on radiative stretching cylinder with Soret and Dufour effects, *Case Studies in Thermal Engineering* **13** (2019), 100384, DOI: 10.1016/J.CSITE.2018.100384.

- [49] M. Sohail, Z. Shah, A. Tassaddiq, P. Kumam and P. Roy, Entropy generation in MHD Casson fluid flow with variable heat conductance and thermal conductivity over non-linear bi-directional stretching surface, *Scientific Reports* **10** (2020), Article number: 12530, DOI: 10.1038/s41598-020-69411-2.
- [50] P. Sreedevi and P. S. Reddy, Effect of SWCNTs and MWCNTs Maxwell MHD nanofluid flow between two stretchable rotating disks under convective boundary conditions, *Heat Transfer – Asian Research* **48**(8) (2019), 4105 – 4132, DOI: 10.1002/htj.21584.
- [51] L. S. Sundar, K. V. Sharma, M. K. Singh and A. C. M. Sousa, Hybrid nanofluids preparation, thermal properties, heat transfer and friction factor – A review, *Renewable and Sustainable Energy Reviews* **68** (2017), 185 – 198, DOI: 10.1016/j.rser.2016.09.108.
- [52] H. Upreti, A. K. Pandey and M. Kumar, Thermophoresis and suction/injection roles on free convective MHD flow of Ag-kerosene oil nanofluid, *Journal of Computational Design and Engineering* **7**(3) (2020), 386 – 396, DOI: 10.1093/jcde/qwaa031.
- [53] I. Waini, A. Ishak and I. Pop, Dufour and Soret effects on  $\text{Al}_2\text{O}_3$ -water nanofluid flow over a moving thin needle: Tiwari and Das model, *International Journal of Numerical Methods for Heat & Fluid Flow* **31**(3) (2021), 766 – 782, DOI: 10.1108/HFF-03-2020-0177.
- [54] C. Y. Wang, Stretching a surface in a rotating fluid, *Zeitschrift für angewandte Mathematik und Physik ZAMP* **39**(2) (1988), 177 – 185, DOI: 10.1007/BF00945764.

